Supporting Information

Near-infrared visualisation of single microparticle electrochemistry for batteries

Xinyue Wang, Si-Cong Wang, Junjie Ma, Ruo-Chen Xie,* and Wei Wang*

State Key Laboratory of Analytical Chemistry for Life Science, School of Chemistry and Chemical Engineering, Chemistry and Biomedicine Innovation Center (ChemBIC), Nanjing University, Nanjing, 210023, China

Correspondence: crxie@nju.edu.cn (R.-C. Xie); wei.wang@nju.edu.cn (W. Wang).

--------------------Contents--------------------

Experimental Procedures

Materials and Characterisation

Lithium cobalt oxide ($LiCoO_2$, or LCO) powder was purchased from Sigma-Aldrich; $LiCoO_2$ nanoparticles were obtained by manual grinding. The shapes and sizes of LCO particles were characterised by scanning electron microscopy (Phenom Pro, PhenomScientific, China) and atomic force microscopy (Icon, Bruker).

Optical Apparatus

All optical measurements were performed on an inverted microscope (Nikon, Ti-E, Japan), equipped with bright-field and dark-field condensers. Light Emitting Diodes (LEDs) with wavelengths from the visible to near-infrared region (470 nm, 530 nm, 660 nm, 730 nm, 850 nm, 1050 nm; Thorlabs, USA) were used to illuminate the particles. A monochrome CCD camera (Pike F-032, Allied Vision Technology, Germany) was used to collect transmitted or scattered light through a 20X objective (Nikon, N.A.=0.45) to produce the bright-field or dark-field images respectively. The image acquisition rate is set to be 1 frame per second. Image analysis was performed using Fiji and Matlab R2021a.

Electrochemical Measurements

The $LiCoO_2$ microparticles were dispersed on an indium-tin-oxide (ITO) conducting glass slide by spin coating (EZ4 Spin Coater, Schwan technology, China) a suspension of the particles, on to which a PDMS chamber was firmly attached, serving as the electrochemical cell. Then the cell was dried in a vacuum at 40 °C for 2 hours for immobilizing the lithium cobalt oxide microparticles. 1 M $LiNO_3$ solution with the pH of 10 was used as the electrolyte solution. The electrochemical measurements were performed using a CS310M electrochemical workstation (CorrTest, China) and a three-electrode system. The modified ITO served as the working electrode, a polished Pt wire and a homemade pseudo-Ag/AgCl electrode were used as the counter electrode and the reference electrode, respectively. The ITO electrode was cleaned before use by 15 minutes' sonication in acetone, ethanol and deionised water in sequence.

1. pH dependence of LiCoO$_2$ electrochemical stability
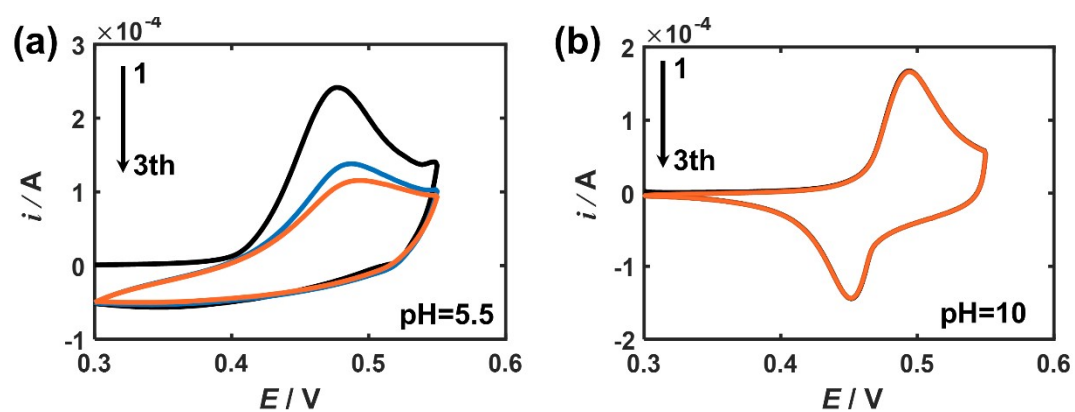
Figure S1. Cyclic voltammetry of LCOMPs ensembles immobilised on an ITO electrode in the 1 M LiNO$_3$ solutions with pHs of (a) 5.5 and (b) 10. Scan rate 5 mV s^{-1}.

2. Discussion for the depth of field

The depth of field defines the distance in the optical axis over which the imaging system produces a sharp image of the object of study on the camera sensor. When the camera resolution (pixel size = 370 nm in our case) is smaller than the incident wavelength (1050 nm), the depth of field (d) is directly proportional to the latter as seen from [1]:

$$d = \frac{n\lambda}{2NA^2}$$

where n is the refractive index of the medium between the objective and the substrate electrode, NA is the numerical aperture of the objective. In this work, the medium is air (n = 1.00) and NA is 0.45, and therefore the depth of field is estimated to be 2.6 µm. When the wavelength of light is switched to 470 nm, the depth of field is still as thick as 1.2 µm, which is expected to be sufficient for most studied microparticles to be 'adequately' focused at the focal plane for sensitive measurements by the optical set-up.

3. Wavelength dependence of measuring a number of LCO particles in an optical field
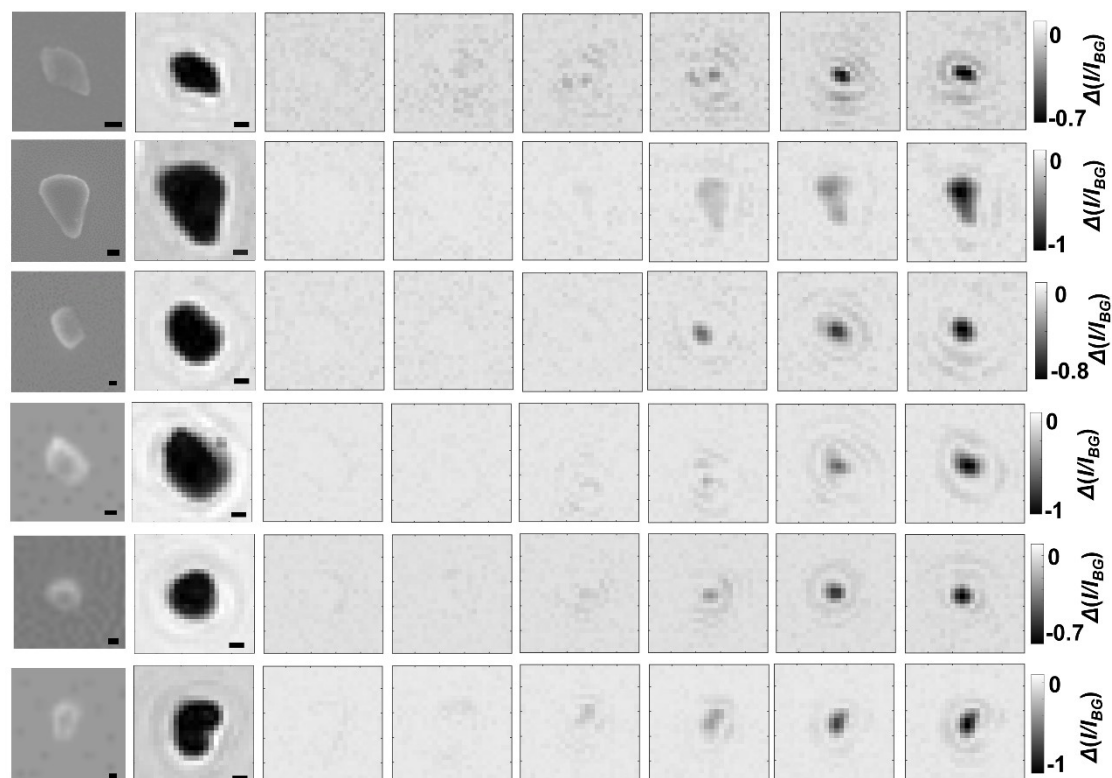

Figure S2. (Left columns) SEM images of six individual single LCO microparticles and corresponding BF images; (Right columns) Corresponding differential BF images between the oxidised and reduced state of each particles at the different incident wavelengths, respectively. Scale bars all 1 µm.

4. Reproducibility of the measured optical transmittance variation
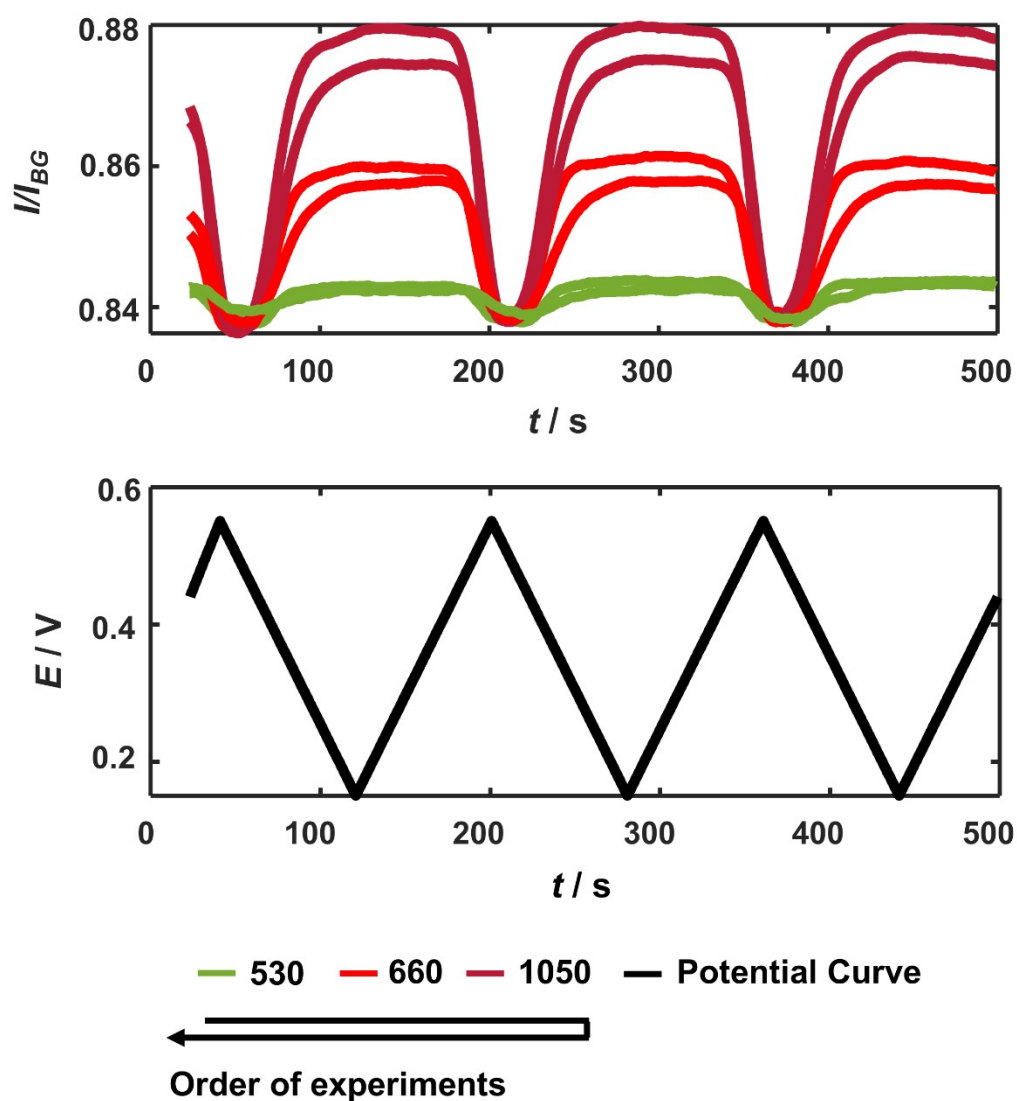

Figure S3. Optical transmittance as a function of time with a range of incident wavelengths between 530 nm and 1050 nm used sequentially (see the arrow for the order of the experiments). Black curve represents the applied potential ramps.

5. AFM characterization of LiCoO$_2$ nanoparticles
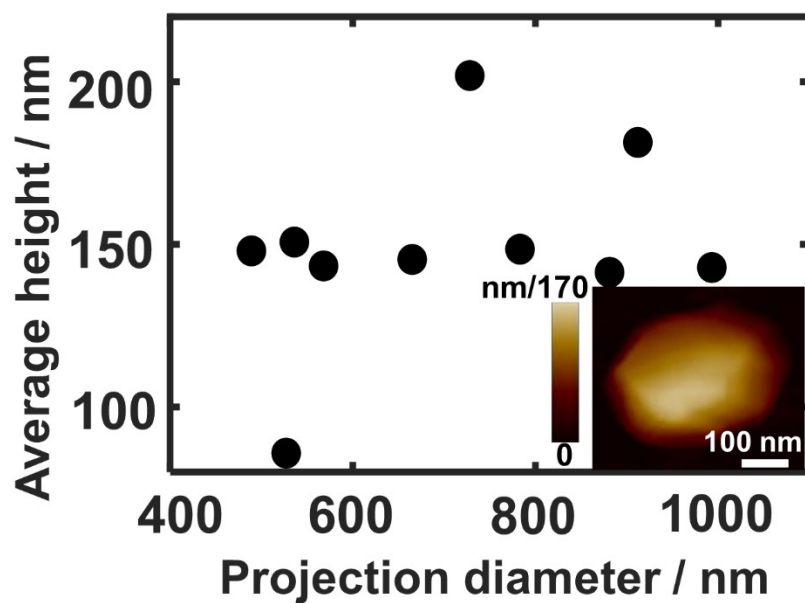
Figure S4. AFM characterisation of LiCoO$_2$ nanoparticles with a projection-area-equivalent diameter of around 500±140 nm and a height of about 150±40 nm.

6. BFM imaging of wavelength-dependent electrochromism of single LiCoO$_2$ nanoparticles
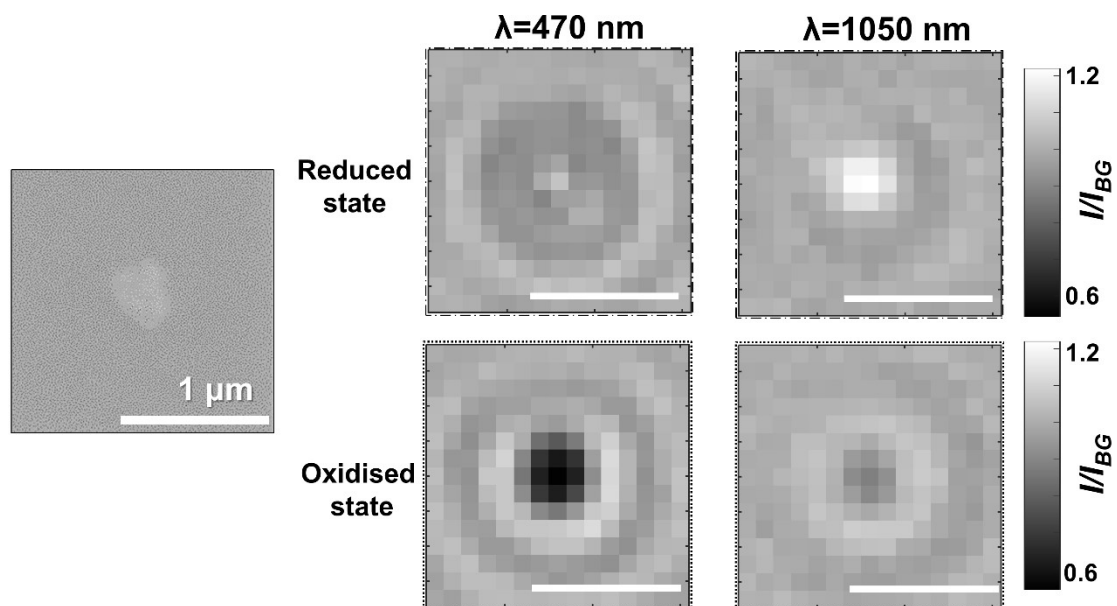
Figure S5. SEM image and BFM imaging of LiCoO$_2$ nanoparticle at its reduced and oxidised state under 470 or 1050 nm illumination, respectively. Scale bars all 1 μm.

7. Wavelength-dependent power absorption coefficients of LCO

Table S1. Power absorption coefficient dataset for a single $LiCoO_2$ macrocrystal [2].

| λ (nm)	β_R (10^2 μm^{-1})	β_O (10^2 μm^{-1})
470	0.23	0.325
530	0.145	0.27
660	0.085	0.24
730	0.07	0.23
850	0.05	0.19
1050	0.03	0.125

8. Optical measurements of single LiFePO₄ microparticles as a function of light wavelength

To check the applicability of near-infrared (NIR) imaging on other materials, we further investigated the optical contrast changes of single LiFePO₄ microparticles (LFPMPs) under different illumination wavelengths. Again, we first measure the voltammetric behavior of the particle ensembles and then compare it with that measured optically using 850 nm light. Figure S6a shows an excellent agreement between the electrochemical measurements and the optical measurements. Figure S6b shows little decrease in the measured charge of both the anodic and the cathodic processes as the potential cycles proceed, suggesting good electrochemical cyclability of LFPMPs. By contrast, when the illumination wavelength decreases from 850 nm to 660 nm and to 470 nm, the particles become less and less transparent (Figure S6c). Accordingly, the magnitude of the optical changes keeps decreasing drastically as the wavelength of the incident light becomes shorter (Figure S6d). These results demonstrate that the imaging capacity of NIR light is independent of the nature of the materials studied and thus show the universality of the NIR imaging.
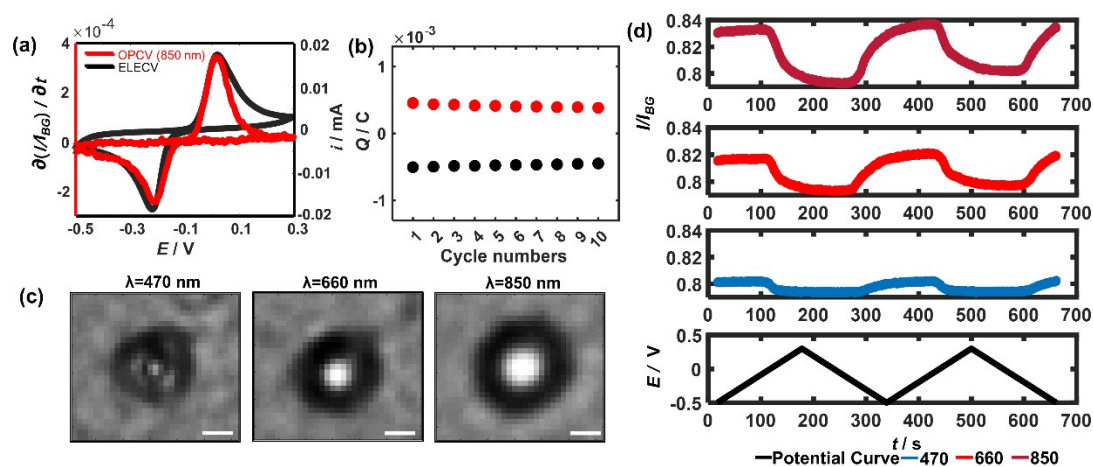
Figure S6. (a) Optical CV curve of individual LFPMP (red curve) and electrochemical CV curve of LFPMPs ensembles on the ITO substrate (black curve). (b) Amounts of charges transferred between the immobilised particles and the ITO electrode during the electrochemical cycling. (c) BF images of individual LFP particles at its reduced state at different incident wavelengths. Scale bars all 2 μm. (d) Optical transmittance as a function of time measured using light with a range of wavelength between 470 nm and 850 nm. Black curve presents the applied potential ramps.

10

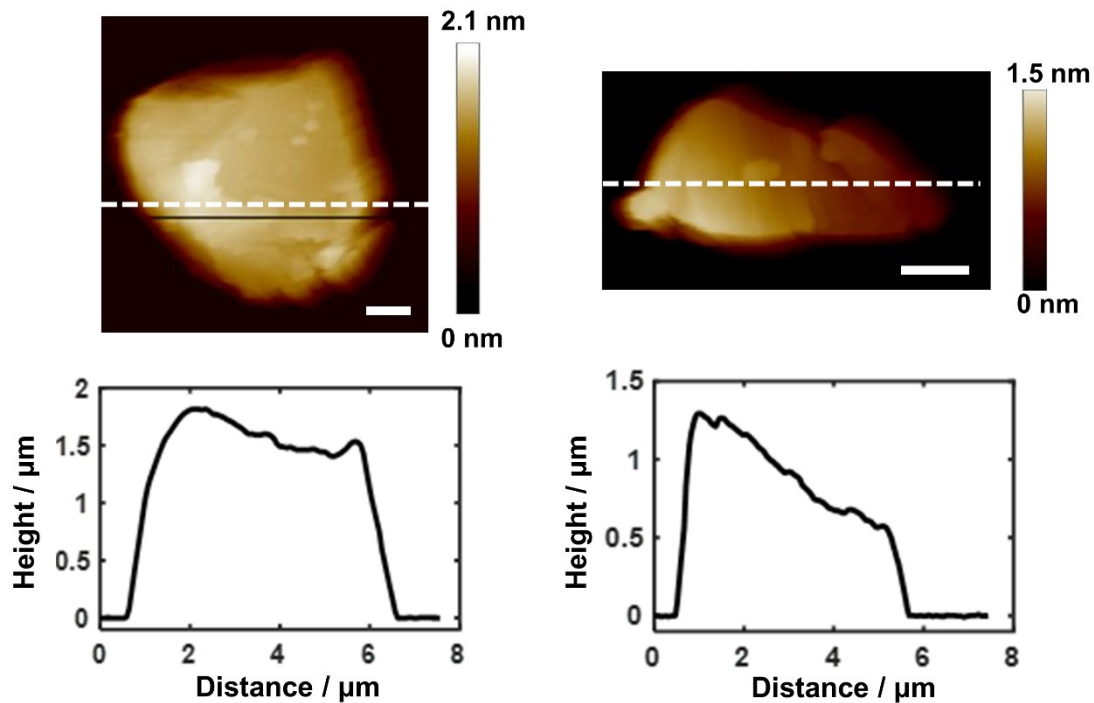## 9. Conversion anisotropy distribution of the single microparticles using BFM imaging
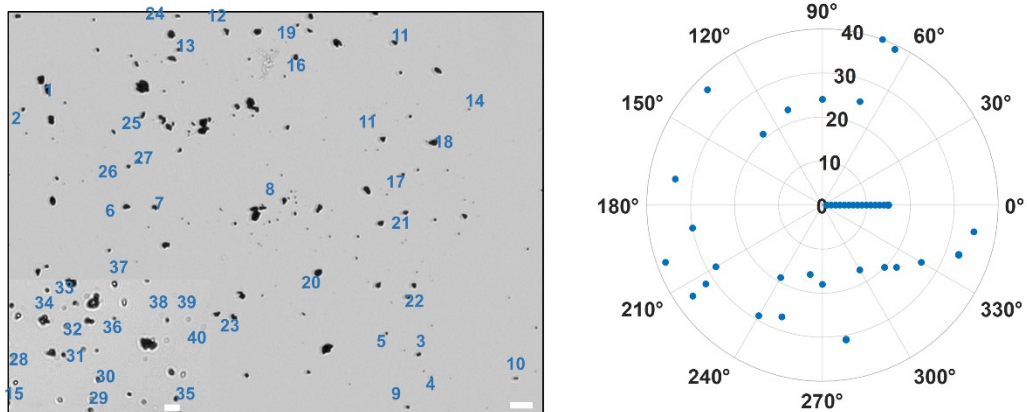
Figure S7. Corresponding BFM image and polar plot of the conversion anisotropy for the measured 40 microparticles. Scale bar 10 μm.

10. Distinct thickness symmetry of LCO particles
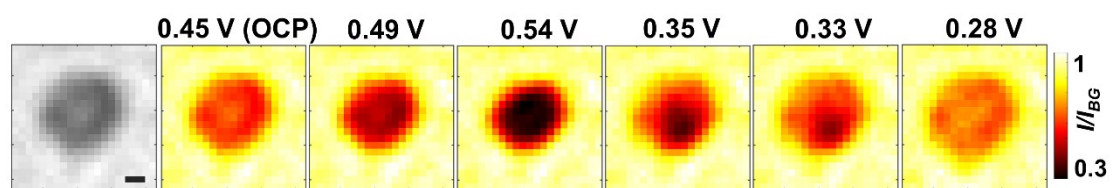
**Thickness variation (mean±STD):**

1460±180 nm;   880±230 nm

Figure S8. Morphology with relatively even and clearly directional thickness of two representative particles. Scale bars all 1 μm.

11. Special case of mixed Li+ diffusion behaviour of a single LCO particle


Figure S9. Corresponding BFM image and serial transmittance mapping of the single LCO particle as a function of the applied potential. Scale bar 1 μm.

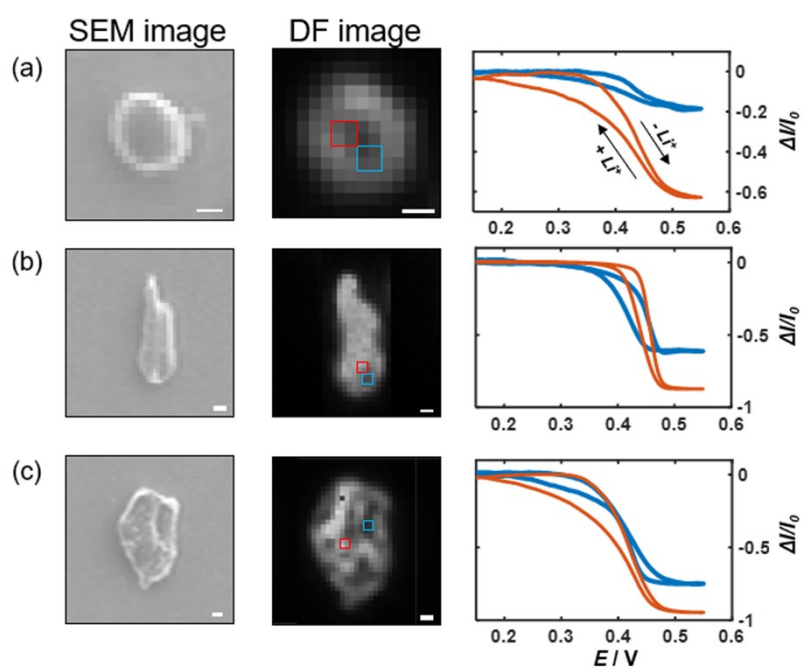## 12. Dark field imaging of single LCO microparticle electrochemistry
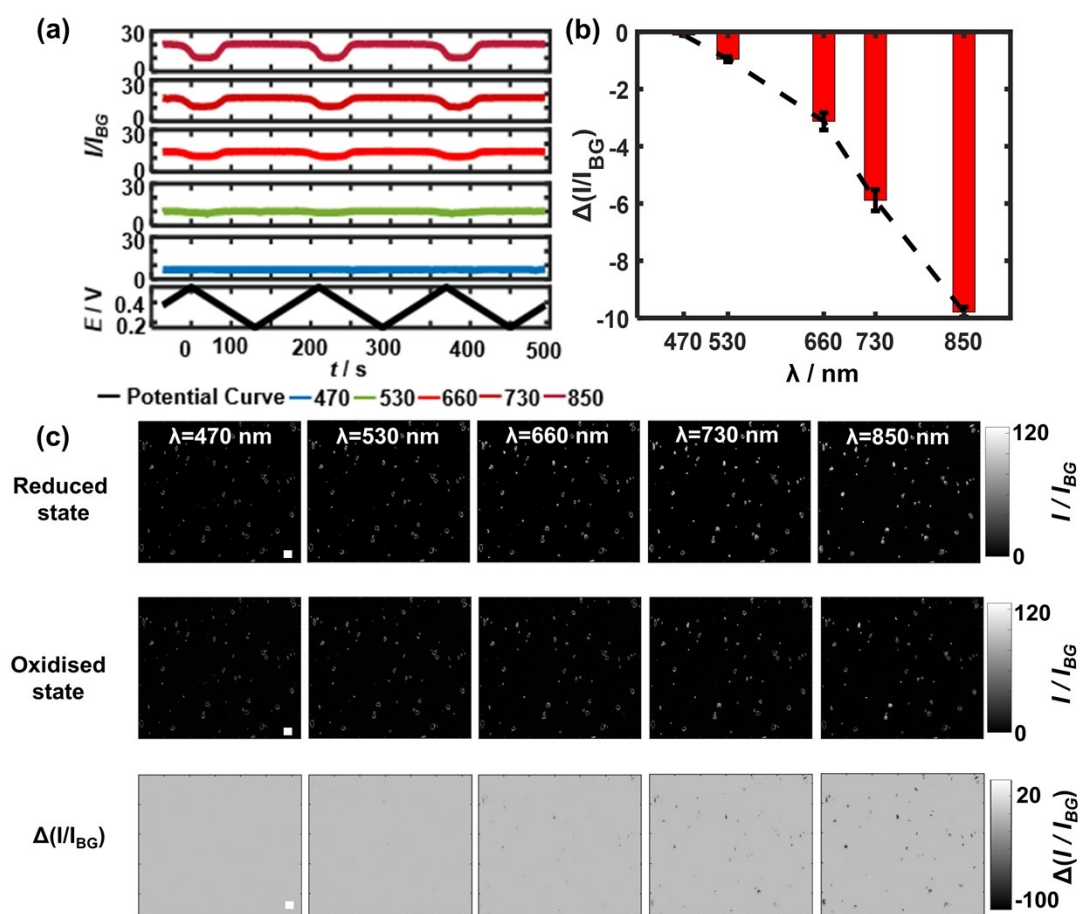
Figure S10. Wavelength dependence of the electrochemical DF intensity (I/I_{BG}) variation of one single LCOMP and (b) the maximum optical contrast changes $\Delta(I/I_{BG})$ as a function of the used light wavelength. (c) The differential DF images (bottom row) of oxidized (middle row) and reduced state (upper row) of all particles in the optical field of view at each incident wavelength, respectively. Scale bars all 10 µm. *Note that (c) is a set of high-resolution images that can be much zoomed in to check the identity of individual 'single' microparticles (as the dark field scattering outlining the particle shape can clearly distinguish).*

13. Conversion anisotropy distribution of the single microparticles using DFM imaging
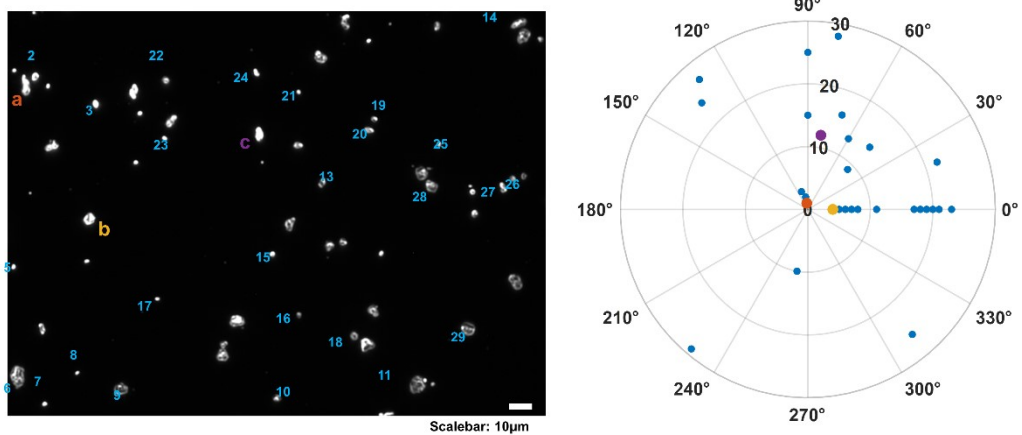
Figure S11. Corresponding DFM image (Scale bar 10 um) and polar plot of the conversion anisotropy for the measured 29 microparticles.

14. Regional reactivity of single microparticles

Figure S12. (a-c) Dark field (DF) scattering, SEM and scattering changes of three single LCO microparticles. For quantifying the scattering changes, $\Delta I / I_0$ is the ratio of measured scattering changes from the initial average intensity to the initial average intensity of the selected ROIs (all consist of four pixels, 0.55 µm^2) in the DF images, as an indicator of the reaction extent. The $\Delta I / I_0$ plateaus at extreme potentials (ca. +0.2 V and +0.5 V) thus correspond to their maximum reaction extents. Scale bars all 1 µm.

15. Directional optical changes of more single LCO microparticles using DFM
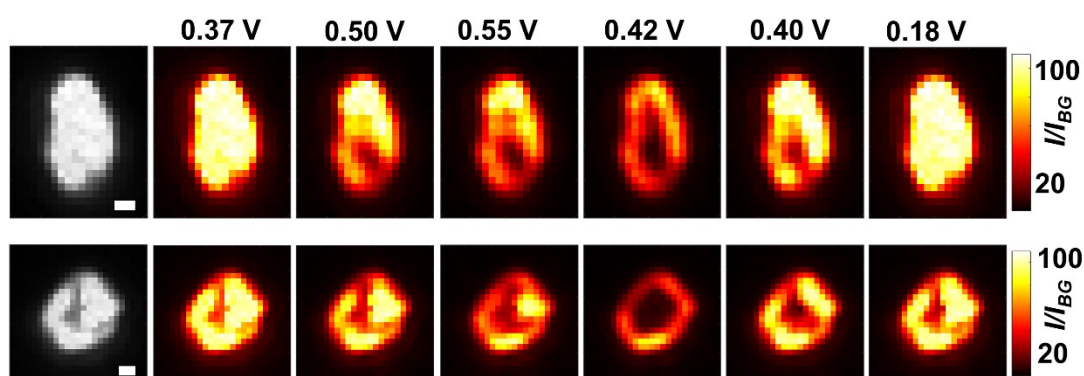
Figure S13. Initial bright-field images of two representative microparticles (leftmost images) at the open circuit potential. Pseudo-coloured images shows the potential-dependent scattered light over the single microparticle using an 850 nm light. Scale bars all 1 μm.

References

1. A. J. Merryweather, C. Schnedermann, Q. Jacquet, C. P. Grey and A. Rao, *Nature*, 2021, **594**, 522-528.
2. H. L. Liu, T. Ou-Yang, H. Tsai, P. Lin, H. Jeng, G. Shu and F. Chou, *New J. Phys.*, 2015, **17**, 103004.